Universität Bonn

Physikalisches Institut

Study of the BGO Open Dipole fringe field and its impact on the momentum reconstruction

Philipp Bielefeldt

Dieser Forschungsbericht wurde als Masterarbeit von der
Mathematisch-Naturwissenschaftlichen Fakultät der Universität Bonn angenommen.

Angenommen am: 19.09.2014
1. Gutachter: Prof. Dr. Hartmut Schmieden
2. Gutachter: Prof. Dr. Reinhard Beck

Acknowledgements

I would like to express my gratitude to my supervisor, Prof. Hartmut Schmieden, for offering me the opportunity to work for him and for assinging me an exciting topic for my work. I appreciate his supportive and spurring manner. I would like to thank Prof. Reinhard Beck for being the second corrector to this thesis.

I must acknowledge all colleagues in our group and the collaboration for all the help and encouraging input to the thesis. A special thanks goes to Jürgen Hannapel and Daniel Elsner for helping with hardware and design ideas. Finally, I would like to thank Valentina Vegna and Thomas Jude for taking time out from their busy schedule to read this thesis and helping me improve it.

Contents

CHAPTER 1

Introduction

Since J. Thomson, E. Rutherford and their colleagues carried out fundamental research on the structure of matter one century ago, our knowledge about the molecules, atoms, nuclei, quarks and other "elementary particles" has been ever increasing—as did the number of unanswered questions. In 1967/68, a collaboration by Stanford Linear Accelerator Centre and the Massachusetts Institute of Technology performed experiments called "deep inelastic scattering" [1] that revealed a complex sub-structure of nucleons made of several particles of light mass dynamically interacting inside the nucleon. Today, these particles are known as quarks and gluons. Of these, six different types are found today (*up, down, strange, charm, bottom, top*), together with their anti-particles.

One of the cornerstones for our understanding of matter are hadrons. In the constituent quark model, they are categorised into "baryons", made of three quarks or anti-quarks and "mesons", composed of one quark and one anti-quark. Additionally, "leptons" exist, which are the electron, muon, tauon and their respective neutrinos. These particles interact with each other by exchange of "bosons", the photon, g, Z and $W^{\pm}$ bosons, [1] together making up the so-called standard model of particle physics.

A remarkable characteristic of quarks—as they are strongly interacting particles—is called "confinement". It means that quarks are never seen in an unbound, free state but only in groups of two or three. The standard model explains this behaviour by requiring that all free particles to be colour-neutral or white in terms of the newly introduced quantum number "colour charge", assigned to every strongly interacting particle, being either *red, blue* or *green*. Every strongly interacting particle consequently must either consist of a complete set of (three) coloured particles (red + green + blue or their anti-colours) or of a pair of coloured and anti-coloured quanta. This effect is theoretically described by the characteristic of the strong coupling constant α_S: α_S asymptotically weakens with increasing momentum transfer between the quarks and decreasing distance. Hence at small distances,

[1] These are the "gauge bosons", for which a good experimental evidence has been established [2], additionally, the higgs-(scalar-)boson has now been experimentally confirmed [3] and a gravitational boson might be found in the future.

smaller than the size of baryons and mesons— typically $\lesssim$ 1 fermi, quarks behave like free particles whilst with increasing separation, their coupling increases so strongly that it finally prevents a separation of quarks, because when the energy spent for separating quarks exceeds a certain threshold, a pair of a quark and its anti-quark will be produced.

Spectroscopy is one experimental technique developed in the late 20$^{\text{th}}$ century to understand the internal structure of nucleons. Hereby the trait of atoms and other composite objects is used to only be able to take on certain "quanta" of energy and hence only being in certain discrete energy states. By measuring these states, knowledge about the electron orbitals and—by hyperfine splitting—the nucleus' magnetic moments can be yielded. To understand more about the internal structure of the nucleons, a promising approach is once again spectroscopy. Protons can be resonantly excited, e. g. using photons in the giga-electronvolt energy-range, as it is done in the *BGO-OD* experiment, and can then de-excite under emission of a meson, just like an atom de-excites under emission of photons. In contrast to the latter, the excitation spectra of nucleons are not as well-described by current theoretical approaches and models. One prominent example is the mix-up in parity and energy of the $P_{11}\left(1440\ \text{MeV/c}^2\right)$ and the $S_{11}\left(1535\,\text{MeV/c}^2\right)$ resonances[2] of the proton. Furthermore, the number of theoretically predicted and expected states considerably exceeds the number of experimentally observed states.

In particular, one important field of interest is the study of vector meson photoproduction off nucleons [4] as well as associated strangeness photo-production [5]. In either case, a good acceptance in forward direction—in the laboratory frame—is required, since the processes are dominated by t-channel exchange at low transfer momentum [6], whilst s- and u-channels contribute little. Experimentally, *low-t* processes result in particles ejected in very forward direction. Hence, in order to investigate these events, a detector with an excellent resolution in forward direction is mandatory.

In Bonn, at the *ELSA* accelerator facility, two experiments are now in place to increase our knowledge on the electromagnetic excitation of sub-nuclear systems: the *BGO-OD* experiment and the *CB-ELSA/TAPS* experiment. Their goal is to understand the baryon spectrum more accurately than before and to investigate the properties of meson-photoproduction reactions.

The *BGO-OD* experiment consists of a central Bismuth Germanate[3] electromagnetic calorimeter with high resolution and angular coverage. It is combined with a forward spectrometer, including a 94 tons open dipole magnet with an central field strength of about 430 mT, delivering a bending power up to $\int B\,\mathrm{d}l \approx 0.74\,\text{Tm}$. The *BGO* crystals are read out using standard photomultiplier tubes, delivering a very pure signal. Since photomultipliers accelerate the electrons created at the photo-cathode via a complex dynode system, they are extraordinarily sensitive to external magnetic fields; hence, one complication in the set-up of the *BGO-OD* experiment is a proper management of the fringe field created by the open dipole magnet of the spectrometer, in order to prevent it from hindering the photomultiplier tubes.

[2] In this $\mathrm{L}_{2\mathrm{I},2\mathrm{J}}$-notation, L refers to the angular momentum (S for l=0, P for l=1, ...), I to the isospin, and J to the total angular momentum.

[3] $Bi_4\,Ge_3\,O_{12}$, a frequently used scintillator material

In this thesis, a way to shield the *BGO*'s photomultipliers from the spectrometer's magnet's fringe field will be discussed, in accordance with its impact on the spectrometer's momentum resolution.

CHAPTER 2

The *BGO-OD* experiment

One of two main experiments at the *ELSA* accelerator facility, run by *Physikalisches Institut* of the Rheinische Friedrich-Wilhelms-Universität Bonn and the state of North Rhine-Westphalia is the *BGO-OD* experiment. The schematics of the *ELSA* facility are depicted in Fig. 2.1: the facility consists of one polarised and one unpolarised injector linear accelerators, a booster synchrotron and the electron stretcher synchrotron, a storage ring that accelerates the electrons to maximum 3.5 GeV. Using this concept, *ELSA* has been the first

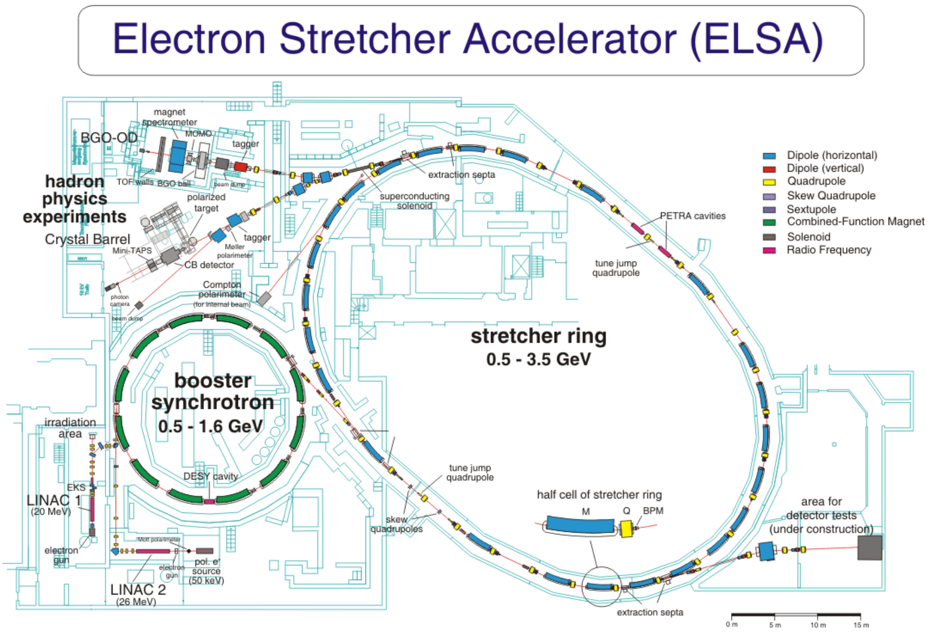

Figure 2.1: Sketch of the *ELSA* accelerator set-up and the position of the experiments. The two main hadron-physics experiments, crystal ball and the *BGO-OD* experiment are depicted in the upper left corner.

operating high duty factor machine for energies up to 3.5 GeV. It delivers a continuous

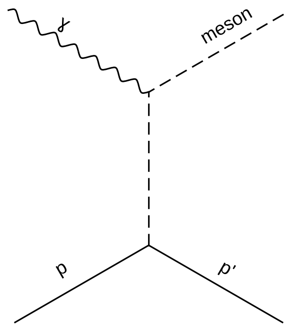

Figure 2.2: A Feynman-diagram of a meson-photoproduction process with a virtual particle exchange in the t-channel, with the time running from left to right.

unpolarised or polarised electron beam of up to 20 nA.

Two main hadron-experiments are currently set up at the facility: the *CB-ELSA/TAPS*-experiment, a crystal barrel detector enhanced with a two-arms photon-spectrometer, investigates the photoproduction of meson resonances to improve understanding of low-energetic QCD.

The *BGO-OD* experiment is designed to carry out research on the photoproduction of mesons off nucleons in order to improve our understanding for the baryon spectra as well as for meson-nucleon dynamics and the strong interaction in particle physics. It does so by combining a *BGO* ball, focusing on the uncharged reaction products, especially photons, with a high-precision forward spectrometer for charged particles. Charged particles can additionally been tracked in the *BGO* ball by using an *MWPC* surrounding the target closely in association with a thin plastic scintillator barrel for $\partial \mathrm{E}/\partial x$ to enable particle identification.

Low-t-Processes

Processes with low transfer momentum are a major experimental subject to the *BGO-OD* experiment. For meson-photoproduction as shown in figure 2.2 the Mandelstam varible

$$t := (p_\mathrm{m} - p_\gamma)^2 = \left(p_{\mathrm{p}'} - p_\mathrm{p}\right)^2$$

can be denoted as $t = \left(M_\mathrm{p} - E_\gamma\right)^2 - \vec{p}_\mathrm{p}^{\,2}$. Low-$t$ in this case confines the proton momentum to values where $\vec{p}_\mathrm{p}^{\,2} \approx \left(M_\mathrm{p} - E_\gamma\right)^2$.

One example reaction studied with the *BGO-OD* experiment is $\gamma\mathrm{p} \rightarrow \mathrm{K}^0\Sigma^+$. Recent data suggest a process as shown in figure 2.3: an intermediate bound state of the kaon and the Λ exist—a $\mathrm{K}^\star$ being produced in the initial t-process and then expelled after exchanging e. g.

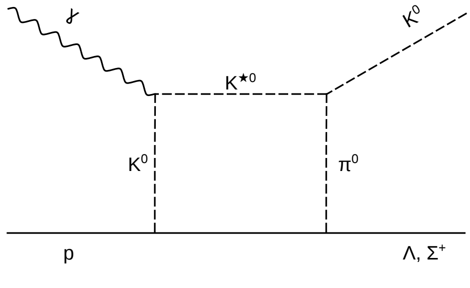

Figure 2.3: A Feynman-diagram of one example process studied in the *BGO-OD* experiment. Before the re-scattering into the observable state, meson-baryon interaction could take place [7]

a π^0 with the Λ. The *BGO-OD* experiment is ideal for this investigation. At low transfer momentum, the kaon travels in very forward direction and is detected by the spectrometer whereas the Λ, decaying into a nucleon and a pion (which itself decays via $\pi \rightarrow 2\gamma$), is detected in the calorimeter ball. Thereby, the *BGO-OD* experiment's set-up allows a complete measurement of the final states.

Compared to similar detector installations, the *BGO-OD* experiment offers a unique possibility to have a combined analysis of the (primarily neutral) remnants in the central detector together with the charged particles produced that the forward spectrometer is able to detect and investigate with high accuracy. For a proton momentum about 1 GeV, the resolution is about 2 %.

2.1 *BGO*-OD's Set-Up

As shown in fig. 2.4, the *BGO-OD* experiment consists of three major parts: the tagging system, the *BGO* calorimeter and the open dipole spectrometer. *ELSA*'s electron beam, entering on the lower-right part of the figure, first hits a thin metal radiator put in place by a goniometer, where real photons are produced by deflection of the electrons in the nuclear electric field—a process known as *bremsstrahlung*, discovered by Williams [8] and described by Bethe [9] in 1934.

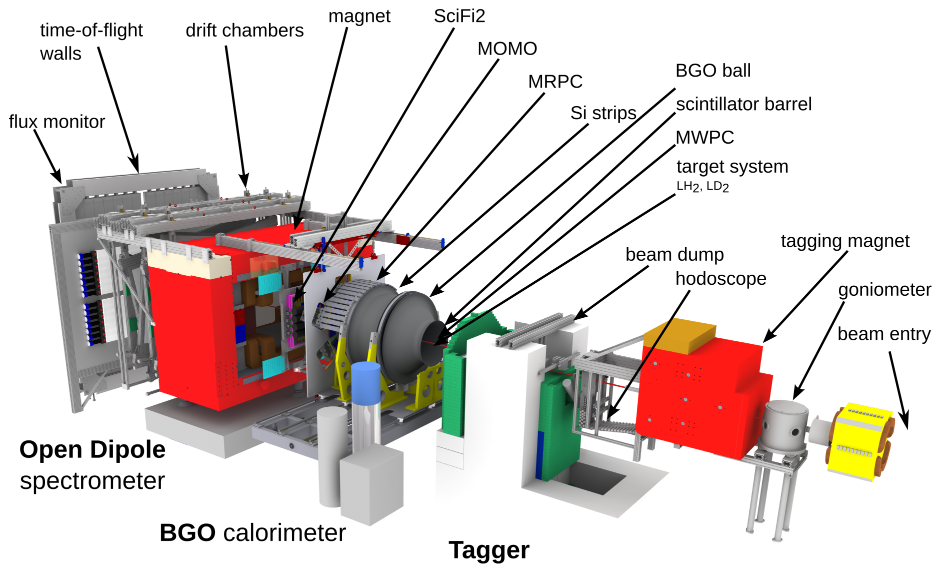

Figure 2.4: Sketch of the experimental set-up at *BGO*: The electron-beam enters at the lower-right side into the tagger, where it is converted into a γ-beam for experiments in the bismuth germanate ($Bi_4\,Ge_3\,O_{12}$) ball. Up-left: The forward spectrometer with its large open dipole magnet.

A tagging system is used in order to know the energy of the created photon (cf. lower right corner of picture 2.4): it consists of 120 scintillator detectors, suited for measuring the energy of bremsstrahlung electrons. Thus, the photon's energy can be calculated by energy conservation. After collimation, the photon-beam impinges upon a cryogenic target in the centre of the *BGO* ball, typically filled with liquid hydrogen (i. e. protons) or deuterium (protons & neutrons). Here, it can interact exchanging a virtual particle with the target nucleon or exciting it.

The *BGO*-Calorimeter

Composed of 480 $Bi_4 Ge_3 O_{12}$ crystals, each of them 24 cm long ($\gtrsim$ 21 radiation lengths), the *BGO*-detector covers an angular range from 25° to 155° around the interaction point optimised for photon and electron detection and also suited for hadrons.[1] To each crystal, a photomultiplier tube[2] is optically connected to convert the *BGO* scintillator light into an electric signal. The *BGO* ball is ideal for measuring photons via electromagnetic cascades and for identifying neutral mesons which decay to photons. It is supported by a scintillator barrel measuring the specific ionisation and a multiwire-proportional-chamber that enables charged particle identification. It is organised in 15 "crowns", denoted by Θ =1 to 15, each a 2π-ring around the beam axis with $\Theta = 1$ being the most downstream crown. Each crown consists of 32 crystals and photomultipliers, numbered with $\Phi = 1$ to 32, ordered counter-clockwise starting from the right side (in beam direction).

All PMTs are cased in a highly permeable metallic cylinder to shield them against perpendicular components of external magnetic fields. Nonetheless, the spectrometer magnet's field can reduce the efficiency of the tubes, since the field strength at the first PMTs' place is still considerably higher than the terrestrial magnetic field, which usually serves as reference field for PMT-shielding. Moreover, they cannot be mounted perpendicular to the field, but are obviously mounted facing towards the interaction point, in individual angles with respect to the magnetic field. The PMTs and the crystals are attached to a carbon-fibre structure which itself rides on two girders per side, made from ≈4 mm thick construction steel. It is split in two parts along the beam axis so that construction can be done inside the ball. The girders rest on a 4.5 metre long rail system that allows to detach both sides and move them individually.

In the current set-up, the detector's energy resolution is 3 % (FWHM) for 1 GeV-photons [10]. Protons up to a kinetic energy of 500 MeV can also be energetically determined.

BGO calibration

Calibration of the electromagnetic calorimeter is done with four ^{22}Na sources inside the *BGO* ball in such positions that the calorimeter is illuminated fairly homogeneously. ^{22}Na emits three photons per decay since it decays via β^+, emitting two 511 keV pair-production-photons, to the 1275 keV-state of ^{22}Ne, de-exciting with a 1275 keV photon [11]. An example spectrum is shown in figure 2.5: the spectrum is measured for each of the 480 channels of the *BGO* ball in the crystals' SADCs[3]. If the scintillator, the photomultiplier and the electronics work fine, the spectrum looks similar to the one shown in figure 2.5: a small, pronounced peak at low raw ADC values and two broader peaks at higher ADC

[1] In fact, low-energetic protons can be stopped within the *BGO* ball.
[2] Hamamatsu types R329-02 for the central part and R580 for the outer crowns
[3] sampling analogue-digital-converter

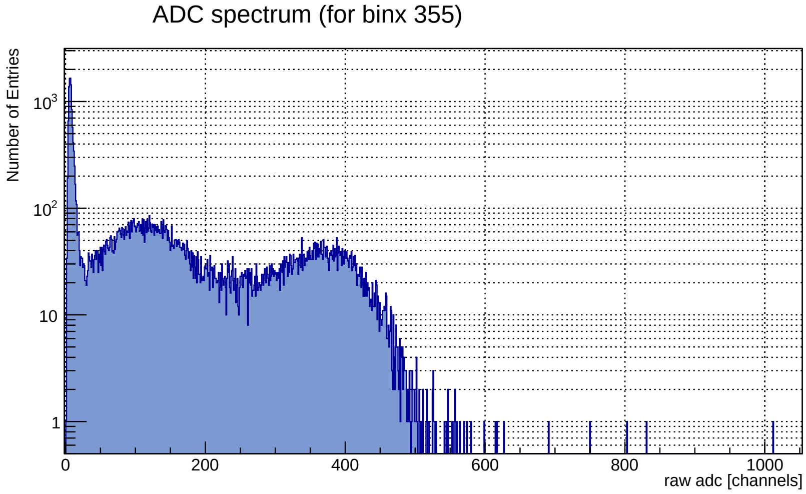

Figure 2.5: An example spectrum of the sampling ADCs at a calibration run. Shown is a ^{22}Na-spectrum, with the 511 keV-line around ADC channel 100 and the neon's 1275 keV-line around channel 385.

values (corresponding to higher energies). In total, the spectrum can be fitted by the sum of five functions, an exponential background plus the two characteristic lines as well as the lines' Compton background. The lines have a Gaußian shape, the Compton background is fitted by a S-function, an integrated Gauß-function.

The peak position of the 1275 keV-γ-line in raw ADC channels (called "*peak_2*") is used as reference point for the calibration procedure. During the *equalisation* process,[4] usually carried out once after setting the magnetic field, the high-voltage supplies of each PMT are set in order to achieve homogeneous *peak_*2-positions for all channels. To map the "raw ADC" value to an actual particle energy, the *calibration* algorithm calculates the energy per ADC-channel for each channel by comparing the *peak_*2positions to the (known) energy of the line (1275 keV). During that process, since the ^{22}Na-lines are at low energies compared to the energies dealt with in the data acquisition, the 12 dB attenuators used in the "normal" data taking are not used. A linearity check was performed for the *BGO* detector when used for the *GRAAL* experiment [12] and will be undertaken for the *BGO-OD* experiment as well.

The Open Dipole Spectrometer

For tracking charged particles created in the target by the photon beam, the *BGO-OD* experiment uses a forward spectrometer. The charged particles' tracks are curved in a magnetic field. Using three tracking detectors, the curvature of their path as well as the exact magnetic field they were exposed to is reconstructed. Thus, their momentum can be calculated via the Lorentz force[5] $\frac{\mathrm{d}\mathbf{p}}{\mathrm{d}\tau} = \mathrm{q} \cdot (U_0\mathbf{E} + \mathbf{U} \times \mathbf{B})$ [13]. The forward spectrometer consists

[4] also referred to as *gain matching*
[5] p being the particle's momentum, U its velocity and $F^{\alpha\beta}$ the (contra-variant) electromagnetic tensor

of multiple sub-systems: *MoMo* and *SciFi2* in front and eight drift chambers behind the magnet. *MoMo*, a scintillating fibre vertex detector composed of six modules is used for

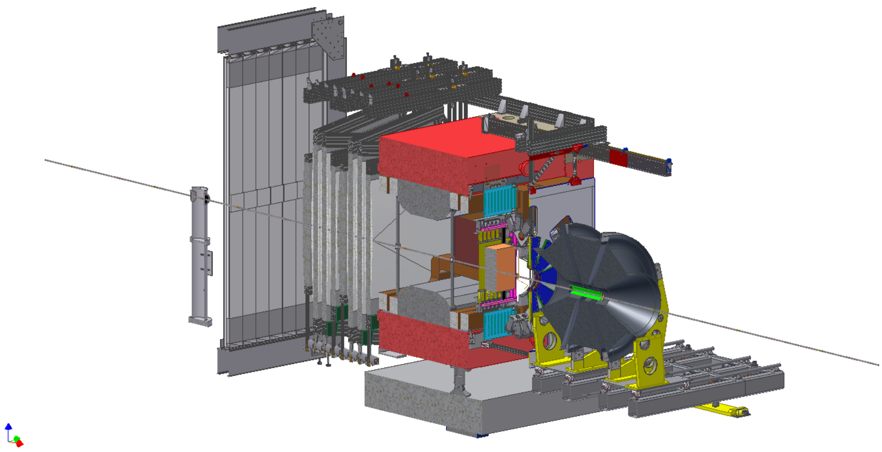

Figure 2.6: Computer drawing of the *BGO* ball and the different parts of the spectrometer: Beyond the multi-wire proportional chamber, MoMo and SciFi2 can be seen, accompanied by the open dipole magnet, the drift chambers and finally the ToF walls

the tracking of particles over a range from 2° to 10°. It is built by 2.5 mm thick scintillating fibres arranged in three layers, read out by 16-channel photomultiplier tubes.[6] These tubes are shielded by a 1 mm mu-metal® cylinder each against the magnet's fringe field. However, this shielding turned out to be insufficient, hence additional 1 mm of Permenorm® was added. *SciFi2* is another scintillating fibre detector, covering a range of ±10° in the horizontal plane and ±8° vertically. It is made of 640 fibres, each 3 mm thick, and read out by 16-channel PMTs.[7] Its task is to deliver the second point (together with *MoMo*) for the track reconstruction of (charged) particles. The particle trajectories are curved by the 0.74 T $\mathrm{m}_{\mathrm{integrated}}$ field in the open dipole magnet.

Drift chambers are mounted downstream from the dipole magnet to complete the tracking of the particles. For each, a double layer of hexagonal drift cells is used, ensuring all tracks hit at least two cells per chamber. The layers are mounted horizontally and vertically and tilted by 9° to remove ambiguities between true and false combinations of multiple hits. This set-up allows the determination of the track direction of the particle incoming to the magnetic field, its position and its outgoing track direction.

By measuring the track direction of the particle "before" and "after" being deflected by the magnetic field, the curvature of the bended particle trajectory can be calculated. Thus, the particle's momentum can be reconstructed precisely, if the magnetic field strength along the trajectory is known well. Details on how the momentum is measured in the *BGO-OD*

[6] Hamamatsu R4760
[7] Hamamatsu H6568

experiment can be found in appendix B.

Information on the time of flight of both charged and uncharged particles, and hence an important measure for particle identification, is measured with the *ToF* detector. Installed at the end of the experimental set-up, 6 m from the interaction point, it covers an angular range of $\pm 12°$ in Θ.

2.2 The Spectrometer Magnet and its Fringe Field

The central part of the spectrometer set-up is the open dipole magnet, permanently on loan from the *DESY* research facility in Hamburg. It is located 2.5 metre downstream from the target. This results in an acceptance of 12.1° horizontal and 8.2° vertical. Its size is (height × width × depth) 2800 mm × 3900 mm × 1500 mm, with a gap of 840 mm × 2330 mm × 910 mm, the total weight is about 94 t.

The non-superconductive coils can be operated with a maximum current of 1.3 kA, delivering a maximum magnetic field of 540 mT in the centre. Figure 2.7 shows the intensity

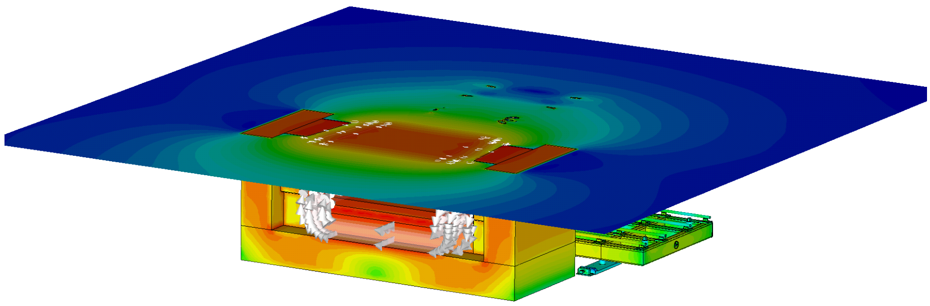

Figure 2.7: Result of the field simulation (absolute field strength) carried out using *CST* Studio®; Depicted is the central plane (cut) through the set-up. In the back part, the *BGO* stands can be seen.

of the magnetic field in the horizontal (x-z) plane at the height of the beam ($y = 0$). At the *BGO*'s first crowns, the total field strength is 2.5 to 3 mT, which is small compared to the field in the magnet's yoke but about 60 times higher than the terrestrial magnetic field.

This has lead to complications with the PMTs used with the *BGO* ball: because of their working principle, photomultiplier tubes are very sensitive to magnetic fields, since these detract the electrons from their design path through the dynode system. Hence, a proper magnetic shielding is mandatory for the operation of PMTs, especially if they are mounted close to a magnet, as is the case in the *BGO-OD* experiment. *By design*, they are not meant to be operated far above the "normal"—terrestrial—magnetic field usually well below 100 µT.

2.3 Efficiency Measurement

The effect the magnetic field has on the photomultipliers used for the *BGO* can be studied by comparing plots like the one in figure 2.8: It depicts the response (and therefore the efficiency) of each photomultiplier channel during a calibration run. To obtain this information, the expected spectrum (of the sodium source used for calibration, cf. section 2.1 for details) is fitted. From the position of the 1270 keV line in ADC-values in this fit, the total gain can be derived and hence, it is seen whether or not energy is “lost” due to—for instance—an inefficient photomultiplier tube. This information is plotted for every PMT: On the x- or Φ-axis, the number of a *BGO*-crystal and its PMT is shown, Θ, denoted in y-direction, names the crowns’ numbers. Hereby, $\Theta = 0$ refers to the most downstream PMTs.

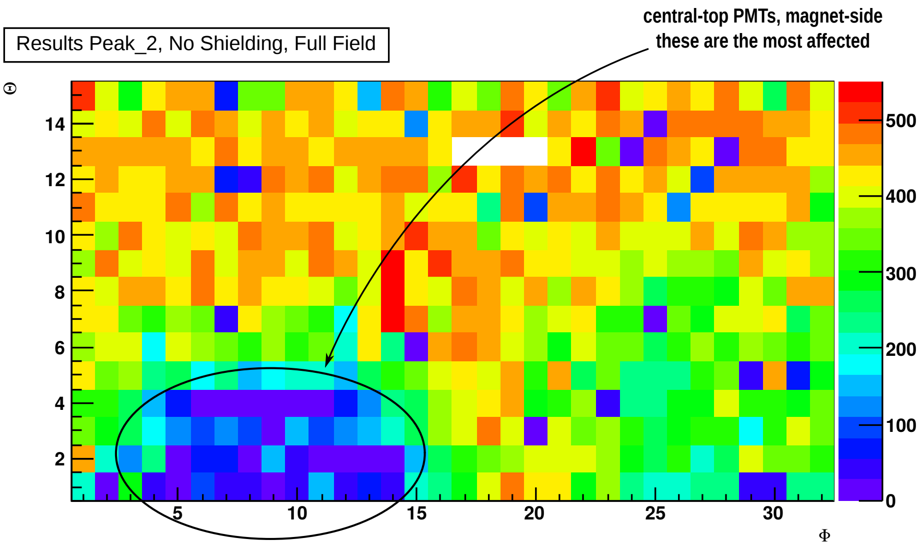

Figure 2.8: Response (in ADC-Channel/MeV) of the *BGO*-PMTs at full field, the bottom-left part is where the PMTs suffer the most losses in energy

From the plot in figure 2.8, it is easily seen that the front crowns is affected most from the fringe field, whilst the more upstream crowns—with more distance to the magnet—are less affected, a behaviour that is expected. Beside that, the lower PMTs of the first crowns (e. g., $\Phi = 16$–32) are less affected than the upper half. To understand why this is the case, a study of a simulation of the magnet’s field was undertaken, as described in section 3.2.

Field Deflection

It was hypothesised that the footing, rail system and the holding structure—all made of steel—deform the magnet’s fringe field. This effect results in a field that is about four times weaker at the place where the lower PMTs of the first crown are placed in comparison to the field strength in the upper half.

A more thorough analysis of the impact of steel shielding concepts can be found in appendix A. From figure 2.8 it is supposed that the shielding provided by the stands makes a huge difference in the detector’s efficiency. Therefore, a solution was demanded that applied a similar detraction to the upper half of the magnetic field, in order to protect the photomultipliers Φ 3 to 14 in crowns $\Theta = 1$ to 4 from the fringe field.

CHAPTER 3

Design of the Magnetic Shielding

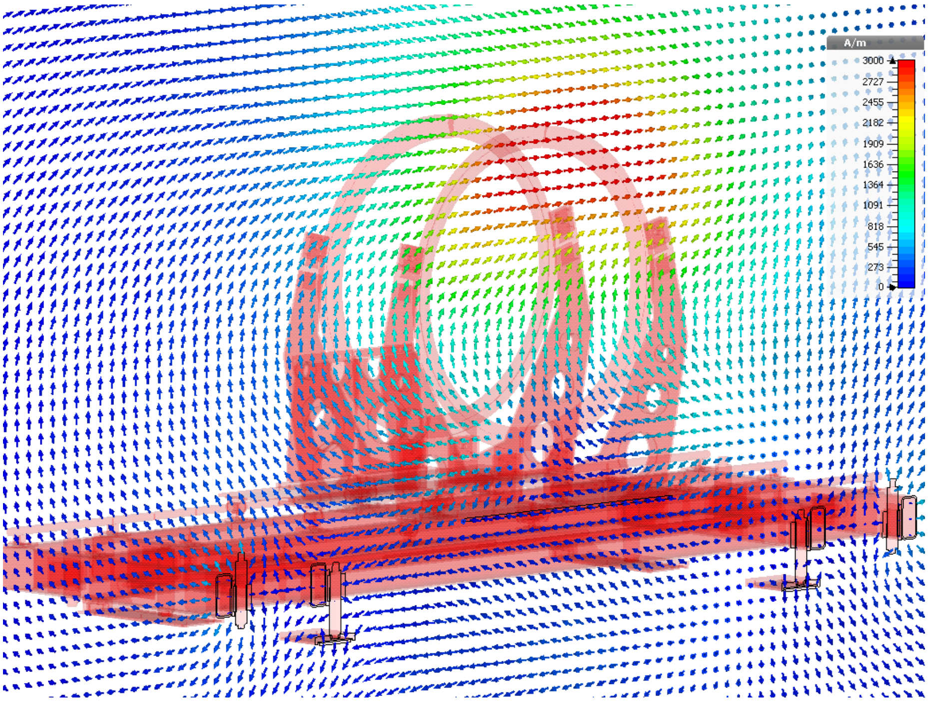

Figure 3.1: Plot of the magnet's fringe field at maximum coil current. Plotted is the magnetic field strength in the plane of the first crown. From this plot, the stands' impact on the field can be studied.

As described in the previous chapter, a shielding capable of drawing the fringe field from the upper photomultiplier tubes was needed for the *BGO-OD* experiment, in order to improve efficiency of both the PMTs and the spectrometer. From field maps such as the one depicted in figure 3.5 and three-dimensional pictures of the field (fig. 3.1, it was hypothesised that the shielding should have some similarities compared to the stands as they seemed to be an effective mean against the field. But since the holding structure's geometry is rather complex, an uncertainty remained on which part of the design are crucial for the shielding effect.

In addition, since the photomultiplier tubes' dynodes' orientations were unknown, it was unclear how the most efficient deformation of the field had to look like. Therefore, multiple designs were simulated using *CST* Studio® and probed with regard to their potential in lowering the magnetic field at the PMTs' positions.

3.1 Shielding Options

All possible designs have to fulfil certain criteria. The shielding must be attachable to the *BGO* ball or another component of the set-up and may not hinder the ball to be opened and moved. Cables for power supply and signal transportation from the crystals/PMTs have to be able to pass the shielding. And finally, the thermal power produced by the experiment requires an efficient cooling which the shielding may not distort inappropriately.

In figure 3.2, two design studies are shown, that were not pursued. Later, a modified solution was found, as shown in figure 3.3. These three design options are described below.

Perpendicular Rows

Initially, tests were made using rows of iron, bent at the detector's outer curvature. This is depicted in figure 3.2a. Since the material is mainly perpendicular to the direction of the field lines, the magnetic field was not well-caught by the iron bars. In this arrangement, the field lines have to "hop" from one row to the next, limiting the shielding's efficiency. Hence, its effect on the PMTs performance was minimal.

From the simulation, it was concluded, that the field has to be "captured" in forward (i. e. beam")""direction. It creates a closed loop through the (upright) coils of the magnet, being—if not influenced—almost horizontal at the first crown's position. The shielding hence needs to provide a low-conductive path from the *BGO* metallic frame back to the magnet, past the PMTs.

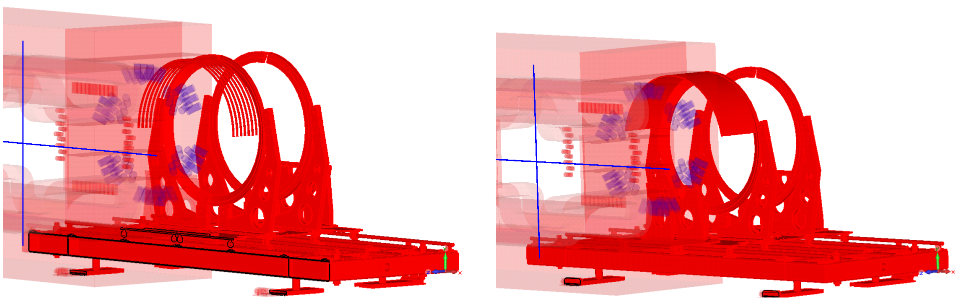

(a) Banded Tubes (b) Cylindrically Curved Plate

Figure 3.2: The two first concepts for the shielding were the "banded tubes" and the cylindrically curved plate.

Curved Plate

The second option which was discussed and simulated, is the cylindrically curved plate, is shown in figure 3.2b. It consists of a massive plate, curved in a way that it fits to the curvature of the *BGO* ball's outer shape and covers the upper part of the detector's downstream front. Advantageously, in this design no gaps are left and hence no edges, at which the magnetic field could potentially show unexpected and unwanted behaviour.

From the simulation of this design it was learned that an undivided shielding does catch up a lot of field lines but hereby potentially gets into saturation. The shielding's efficiency suffers substantially—compared to a divided design, with the same amount of material used for shielding, the field strength in the z-direction as well as the absolute field strength at the photomultiplier's position are about twice as high. Hence, either a thicker shielding or a more complex design of multiple, isolated parts is required. The latter has the advantage of being more lightweight and hindering the *BGO*'s cooling and accessibility less.

Parallel Bars

To avoid the difficulties with the curved plate ansatz, the design was altered to a construction of 24 individual bars, each $70 \times 20 \times 500\,\text{mm}^3$ in size and arranged as shown in figure 3.3. Being separated by 20 mm, the bars are well-isolated against each other and op-

Figure 3.3: CAD-Drawing of the 24 bars of the shielding close to the final design

erate below their saturation magnetic flux. They draw the field into themselves, bending it from the photomultiplier tubes placed below them and cause the field to "flow" around the area in which it has the most harmful impact. From figures such as [3.4], it was understood that this kind of shielding deforms the magnetic field, strengthening it outside the critical area but reducing its strength where the PMTs are located.

Mounted onto an aluminium arch that is fixed to the girders at both sides, the bars are kept in place, leaving a ≈ 30 mm gap between the individual bars and the other components of the holding structure open. From studies on the simulation results, it was understood that this gap noticeably reduces the shielding's effectiveness.

Hence, the upper twelve bars were moved approximately 50 mm upstream, far enough to overlap with the girders,[1] and the remaining vertical gap of $\approx$ 10 mm was filled with blocks of steel to optimise conductivity. The simulated magnetic field, as deformed by this shielding, is shown in figure 3.4.

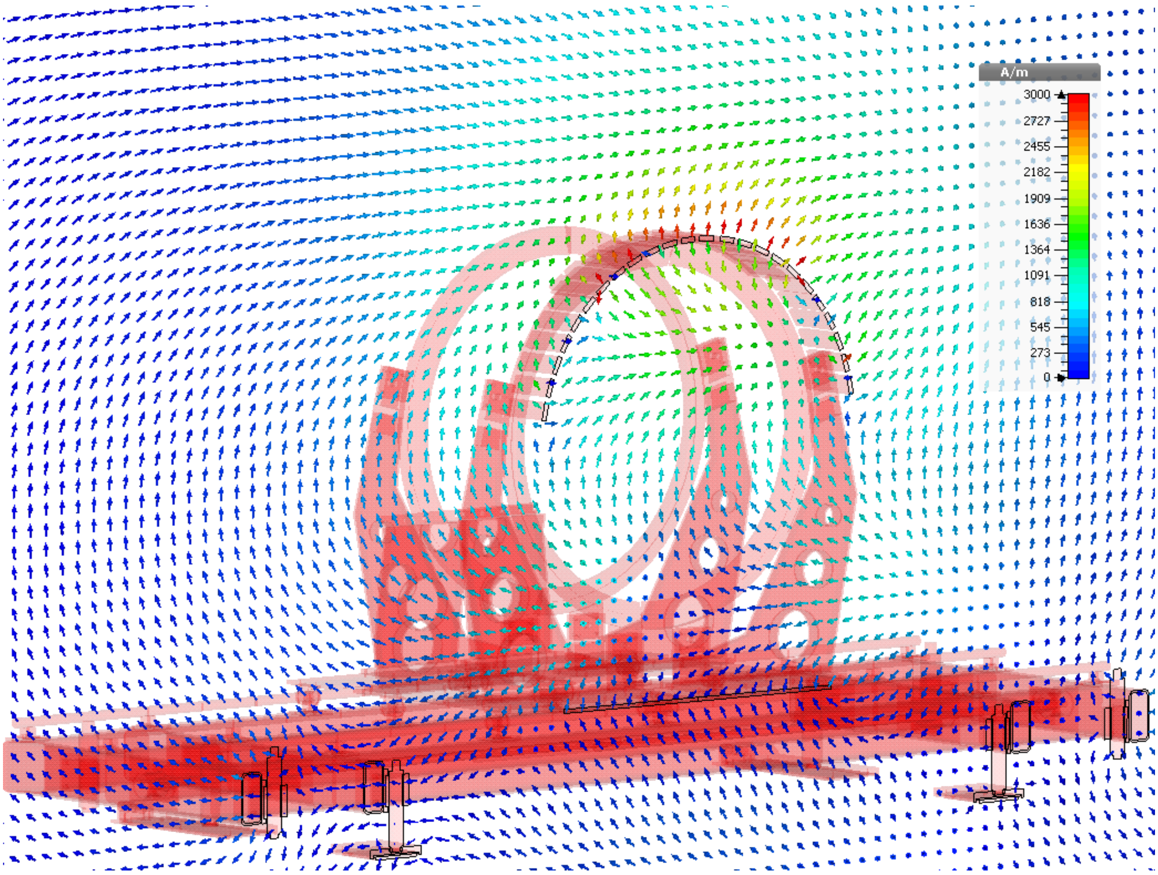

Figure 3.4: The shielding's distortioning impact on the magnetic field can be seen in field maps, where the (real part of the) magnetic field at full coil current is plotted in 3D; The picture above shows a cut trough the experiment at the central position of the first crown with the magnetic field, as fig. 3.1 showed for the non-shielded case.

[1] For the lower 2×6 bars, moving was impossible due to technical constraints.

3.2 Simulation of The Magnetic Field

All different shielding designs were investigated using the electromagnetic simulation results of *CST* Studio® [14], a common simulation programme. It uses a finite element method to solve Maxwell's equations in a hexahedral mesh of typically 50 to 500 M cells, with an auto-adjusted granularity. From the CAD designs, the experiment's geometry is mirrored in *CST* Studio®, then simplified to help the simulation speed. The characteristic electromagnetic properties are used from an internal library.

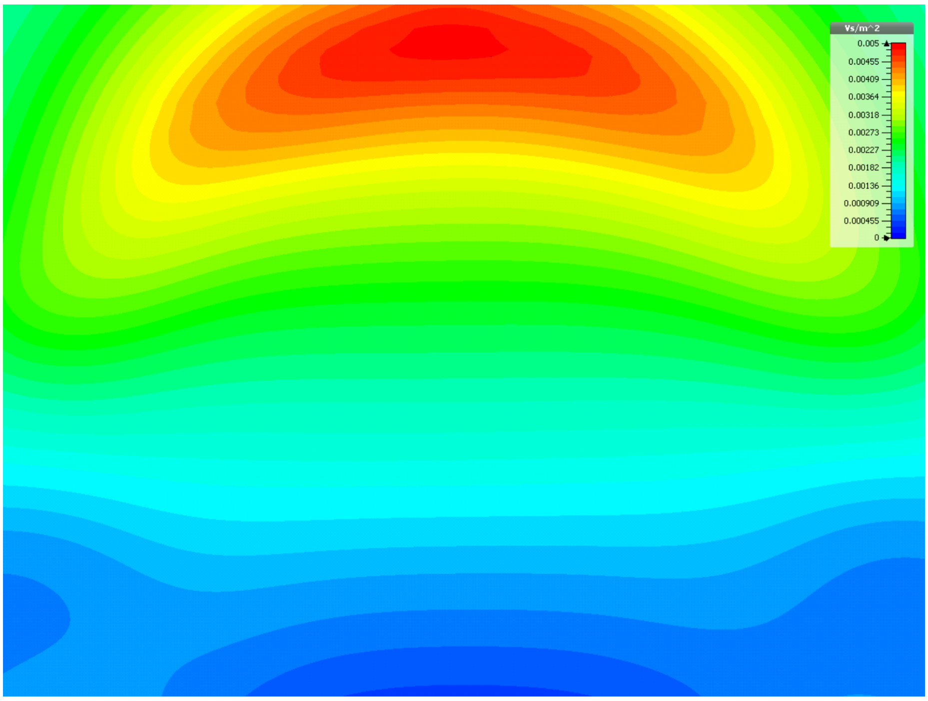

Figure 3.5: Resulting field map of a *CST* Studio® simulation at maximum coil current at the position of the first *BGO* crown with no shielding added: The fringe field is significantly higher for the upper part of the detector

A typical simulation takes 60 to 90 hours on a quad-core, 3.4 GHz (Intel i7-4770®) machine. The result is depicted in figures 2.7 and 3.5. The former shows an overview of the magnet's field in the x-z-plane, the latter (perpendicular to it) a field map in the x-y-plane at -2230 mm, corresponding to the average position of the first crown. Figure 3.5 shows the absolute magnetic field strength at maximum coil current in the plane of the first crown (cf. fig A.1a), where in the lower part, the stands are located (not shown in the plot), while the upper half does not profit from extra material. The field's profile shows that it is distracted and more curved in the lower half, a possible reason for it to be weaker here.

Including the shielding, as shown in figure 3.6, weakens the absolute magnetic field strength where the photomultiplier tubes are located by 60 %.

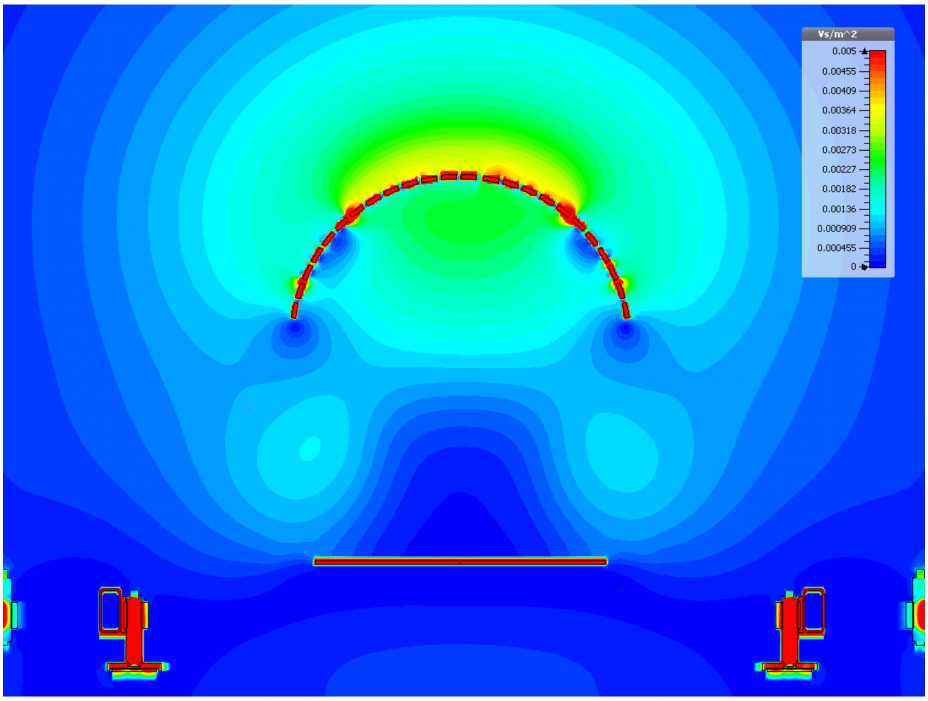

Figure 3.6: Resulting field map of a *CST* Studio® simulation at maximum coil current at the position of the first *BGO* crown with the final shielding (compare to fig. 3.5)

3.3 The Shielding's Influence on Particle Momenta Reconstruction

Deforming the field as described before, does have an influence on the momentum reconstruction. In the *BGO-OD* experiment, the momentum of the charged particles emitted from target, leaving the *BGO* ball in the forward direction is measured by the spectrometer. It uses the deflection of charged particles' tracks in magnetic fields: The particles—for instance, kaons and protons—move along a straight track if not exposed to a magnetic field, but the track is bent depending of the integrated magnetic field the particles are exposed to between the interaction point and the detectors. More detail on the momentum reconstruction can be found in appendix B.

Two different kinds of inaccuracy concerning the magnetic field were investigated that can occur due to the installation of the magnetic shielding: Since the magnetic field is weakened in the central plane and since the shielding deforms the field, the momentum reconstruction could be flawed by assuming a wrong field strength or direction. In order to understand the effect that a modified magnetic field might have on the actual reconstruction accuracy of the *BGO-OD* experiment, the "normal" simulation for the detector efficiency and accuracy was altered. Ordinarily, the software used for simulation and analysis in the *BGO-OD* experiment[2] uses the same field map for the reconstruction of particles that is used for their simulation. The programme was split in two parts, one simulating a particle's

[2] ExPlORA see also appendix B

track and another one reconstructing it. It was made possible to intercept here and use an other field map for simulation than for reconstruction. Thereby, an investigation of the shielding's effect on the particle reconstruction accuracy could be carried out, by using a field map "with shielding" for the simulation of the particle and a field map "without shielding" for the reconstruction.

The analysis software used by the *BGO-OD* experiment, as well as by the *CB-ELSA/TAPS* experiment[3] enables histograms showing differences between acutal simulated momenta and the reconstructed momenta. As a result the so-called "MomentumResolution" [fig. C.1] and "MomentumResolution1D" [fig. C.2] plots are created. The former shows, over the simulated energy range, the relative momentum difference Δp between the simulated and the reconstructed particles. The latter is a projection of the former on the Δp-axis.

There are two major topics related to the magnetic field that were investigated: The dependence of the momentum reconstruction's accuracy on the knowledge of the absolute field and the impact of the fringe field on the momentum reconstruction. These topics may affect the measurement either by the resolution of the reconstruction, or an offset in the reconstructed momentum.

Measuring The Magnetic Field

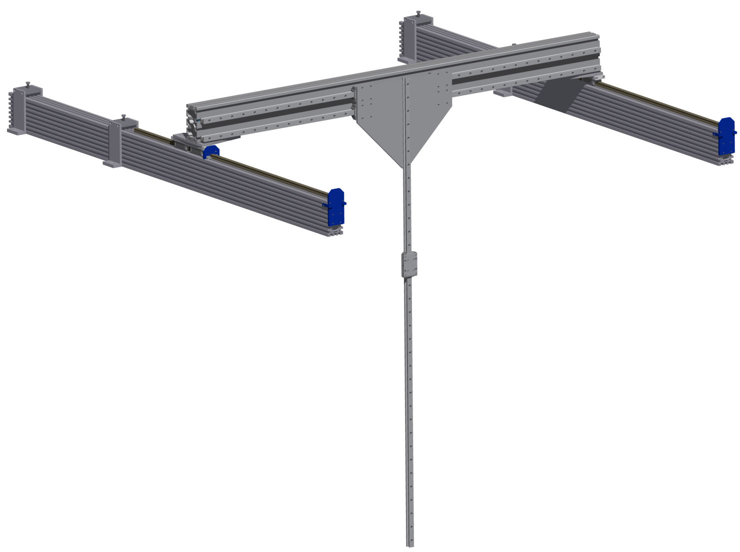

Figure 3.7: A supporting rod to which the Hall probe will be attached for the in-situ measurement of the field map (CAD drawing)

Because of the technique the momentum of particles is detected in the forward spectrometer, it is crucial to have a precise knowledge of the magnetic field. As of now, the data analysis relies on a simulated field map that was cross-checked with precision measurements of the magnetic field done by the *GSI*, but without some of the magnetic parts

[3] More precisely, it's the *Geant* plug-in to ExPlORA, in order to calculate it

installed later at the experiment's place. In order to refresh the field map with higher accuracy, it is planned to do a 3D-scan of the magnetic field in situ.

For the determination of the magnetic field strength, a three-dimensional Hall probe with a precision of up to 30 μT is available. In order to measure the field map as completely as possible, the Hall probe can be mounted on a supporting rod, as depicted in figure 3.7, that itself is moveable by two stepper motors, fixed on top of the magnet. As the absolute positioning that can be achieved by the stepper motors is fairly imprecise, an alternative way to determine the Hall probe's position was investigated. It is planned to make use of a lasertracker system—a Leica® AbsoluteTracker AT901-B®—to measure the Hall probe's location within the detector set-up. The AT901-B allows to measure distances with a accuracy as high as 10 μm.

A programme has been written to do the communication with the lasertracker system in order to control both, the stepper motors' movements and the lasertracker for the position measurements. Some technical issues remain yet unresolved, especially the correct initialisation procedure for the lasertracker, including a calibration for current environment conditions, as well as the communication to the stepper motors. The work on these tasks remains ongoing.

CHAPTER 4

Results

4.1 Impact on The Momentum Reconstruction

Shifts in The Magnetic Field Strength

Since the momentum reconstruction relies on the Lorentz force on the particle, changes in the magnetic field strength assumed for the reconstruction should result in a linear change of the reconstructed momentum. In order to confirm that interdependence, the field strength

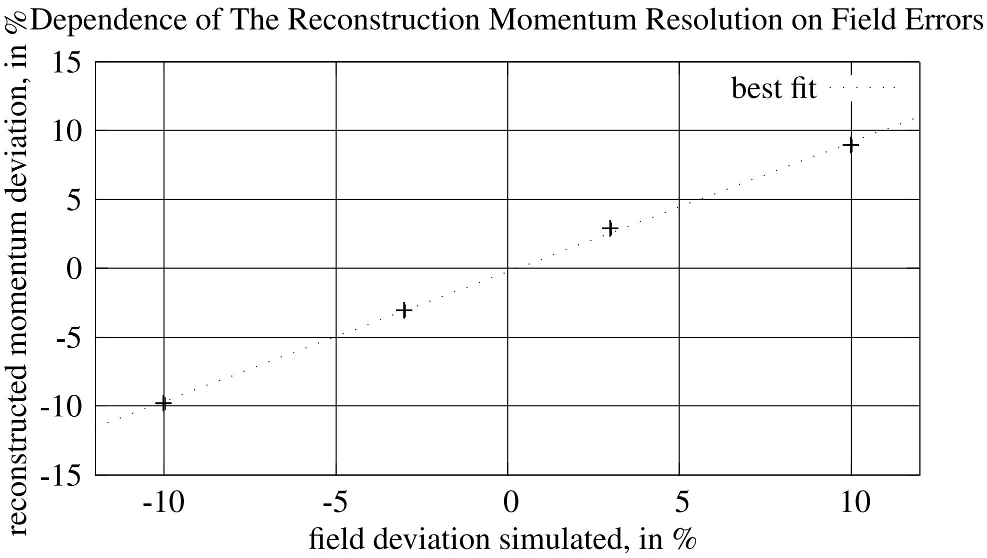

Figure 4.1: Mean values of the MomentumResolution1D-plots vs. the induced shift in the magnetic field used for reconstruction. At least within 10 % around the maximum field strength, the reconstructed momentum shifts linearly with the magnetic field estimate.

for reconstruction was modified in such way that the algorithm over- or underestimates the total field by either three or ten percent. From the MomentumResolution1D-plots, the deviation in the reconstructed momentum was determined. Plotted against the induced shift in the "reconstruction B-field", as in fig. 4.1, a linear interdependence (with a slope of 0.94 ± 0.02) is evident.

Thus, since the absolute magnetic field can be calibrated using processes with known momenta, and safely assuming that no or only little non-linearities occur due to general field shifts, the focus for the momentum reconstruction is to be set on distortions due to an altered fringe field. Since the magnet's field map was measured with high precision by the "Gesellschaft für Schwerionenforschung", *GSI*, in Darmstadt, the shielding applied for SciFi2 has been altered and the new *BGO*-shielding has been added.

Field Distortions by The Magnetic Shielding

The same mechanism used to investigate the influence of an erroneous assumption of the magnetic field strength was used to reconstruct the particles simulated with the currently used field map,[1] but using the simulated field map *with* the shielding included.

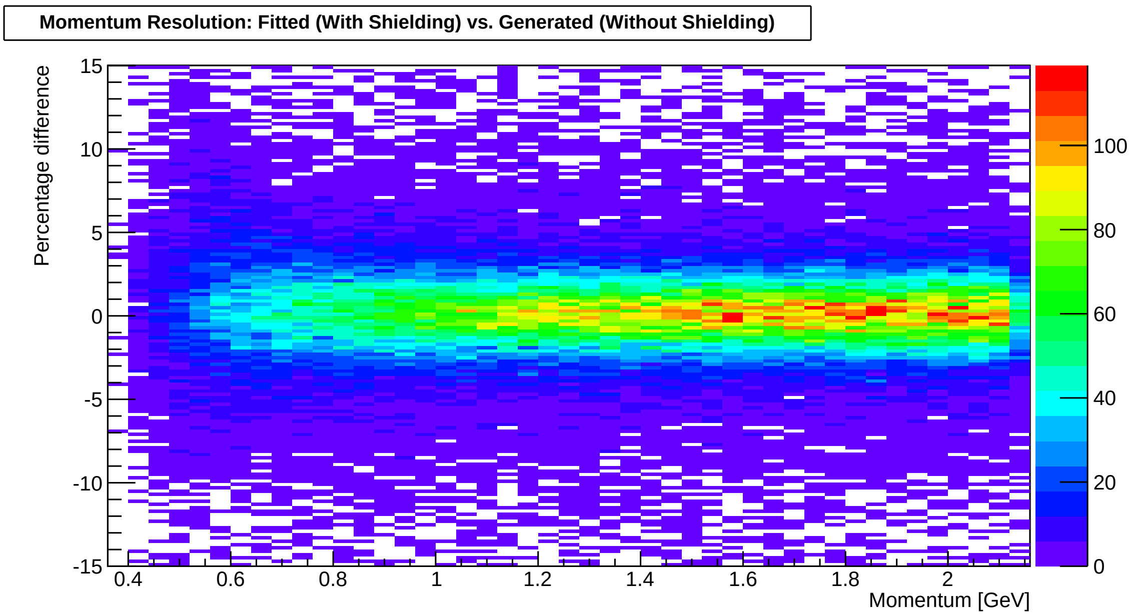

Figure 4.2: Difference in proton momentum for a simulation carried out with the magnetic field *without* shielding by momentum reconstructed for the field *with* the shielding at momenta from 0 to 2.5 GeV

Figure 4.2 shows the deviation between the reconstructed momentum[2] and the simulated momentum. The mean reconstructed momenta does not deviate significantly from the simulated momenta for all values of momentum. The mean of the difference between the fitted

[1] Since measuring the field at some points is practically impossible due to design constraints, for the data analysis, a simulated field map—without the newly added magnetic shielding—is used.

[2] the reconstruction is done using the field map of the simulation *with* shielding, cf. appendix C

and the reconstructed momenta for all values of momenta is close to zero and each distribution is symmetric around its mean. Furthermore, a gradient along the x-axis can be seen, indicating that more particles (in this case, protons were simulated), are detected at higher momenta. To investigate this effect, cuts in intervals of momenta were applied to the plot in figure 4.2, some of them depicted in figure 4.3. These plots show the momentum reconstruction's behaviour for different simulated momenta: the number of entries reduces, whilst the difference distribution[3] gets broader.

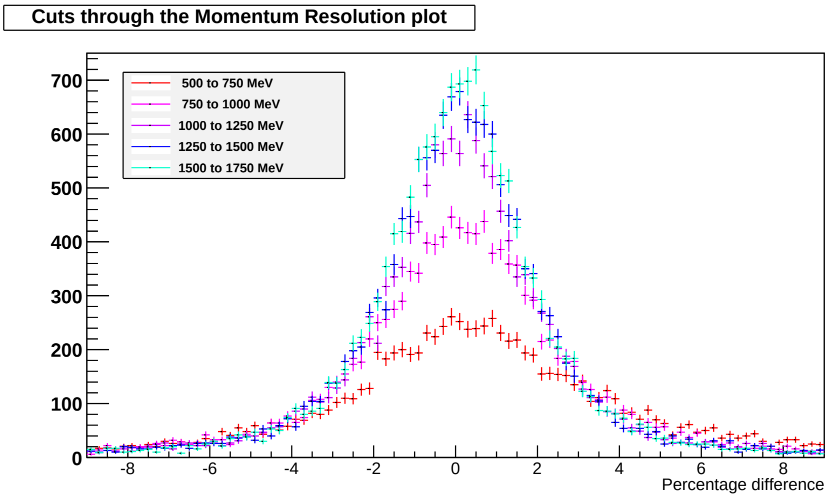

Figure 4.3: Cuts through the Momentum Resolution plot [4.2] at the lower energies, close to the threshold

It was expected that the shielding's deformation of the magnetic field has a larger effect on the momentum reconstruction for low-energetic particles. To scrutinize this hypothesis, the mean shifts in the reconstructed momenta and the width of the distribution shown in figure 4.3 were calculated. The results are listed in table 4.1.

From the second column, it is understood that the shielding's deformation of the field affects particles with low momentum ($\lesssim$ 1 GeV for protons) significantly more than particles with higher momentum—but the total shift in reconstructed momentum, being $< 0.4\,\%$ over the entire range, is small compared to the momentum resolution gained with the forward spectrometer.[4]

An estimate of the forward spectrometer's performance can be derived from the third column in table 4.1: the width[5] of the curves represents the statistical uncertainties for the momentum reconstruction applied to the data. That is, the accuracy—using the full bending power of the magnet—is better than 2 % for particles[6] of 1.2 GeV and above.

[3] The x-axis here is the relative difference (in percent) between the particle's momentum as used for the simulation—done with the field map of the *set*-up without shielding—and the momentum reconstructed by GenFit—with the field map simulated after the installation of the magnetic shielding.
[4] The forward spectrometer has a momentum resolution of $\lesssim 1.5\,\%$, according to Thomas Jude.
[5] being the σ of the gaußian curve fitted to the cuts of the plot in fig. 4.3 in y-direction at different initial momenta
[6] in this simulation, only protons were investigated

Momentum/GeV	**Mean Deviation/%**	**Width** σ**/%**
0.500	0.301 ± 0.094	3.13 ± 0.11
0.750	0.347 ± 0.050	2.47 ± 0.05
1.0	0.0847 ± 0.0303	2.13 ± 0.04
1.5	0.0503 ± 0.0303	1.84 ± 0.03
2.0	0.0924 ± 0.0291	1.83 ± 0.03

Table 4.1: Deviation, caused by the shielding, of the momentum reconstruction: mean and width for different momenta.

Accuracy-Momentum Dependence

The dependence of the momentum reconstruction accuracy on the momentum can be estimated, as shown in figure 4.4. The best fit comes out to be

$$e^{(-2.85\pm0.31)\cdot\left(\mathrm{p}-(0.609\pm0.019)\right)} + (1.79 \pm 0.03)$$

with p being the simulated particles' momenta.

The width of the Momentum Resolution plot (cf. fig. 4.2) changes exponentially with the protons' momenta. The interdependence shown here could be interpreted as a "worst case" scenario, since all field maps used in the analysis might be at least as close to the "true" values of the magnetic field as the two field maps used for this simulation are apart from each other.

A cross-check with the field map currently used for both, simulation and analyses, was performed, in order to eliminate the influence of the deliberate error made in the first simulation. The results of this check are listed in table 4.2. The shifts made in the field map between simulation and reconstruction apparently has only small effects on σ.

Momentum/GeV	**Width** σ**/%**
0.50	3.07 ± 0.13
0.75	2.72 ± 0.06
1.0	2.14 ± 0.04
1.5	1.86 ± 0.03
2.0	1.82 ± 0.03

Table 4.2: Momentum reconstruction width using the same field map for simulation and reconstruction, as comparision to table 4.1

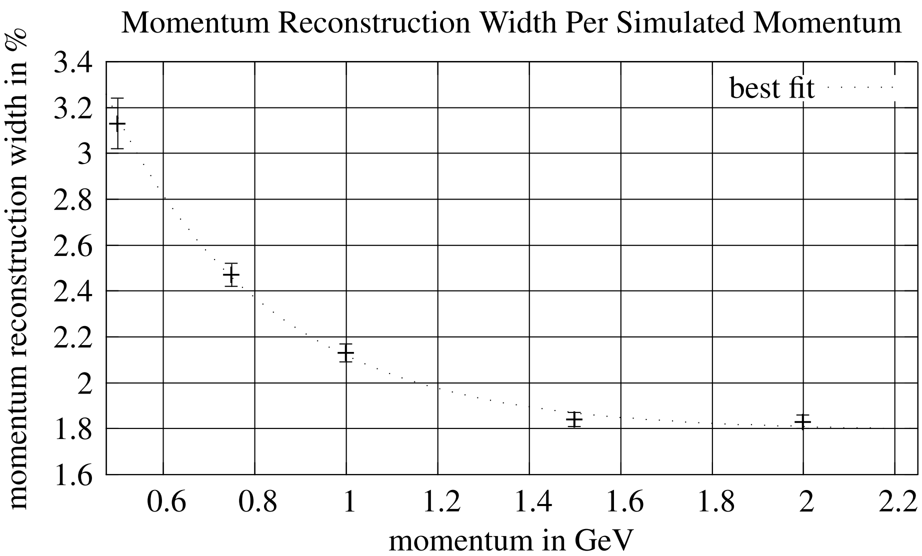

Figure 4.4: Widths of the momentum distributions as shown in fig. 4.3; Cf. table 4.1

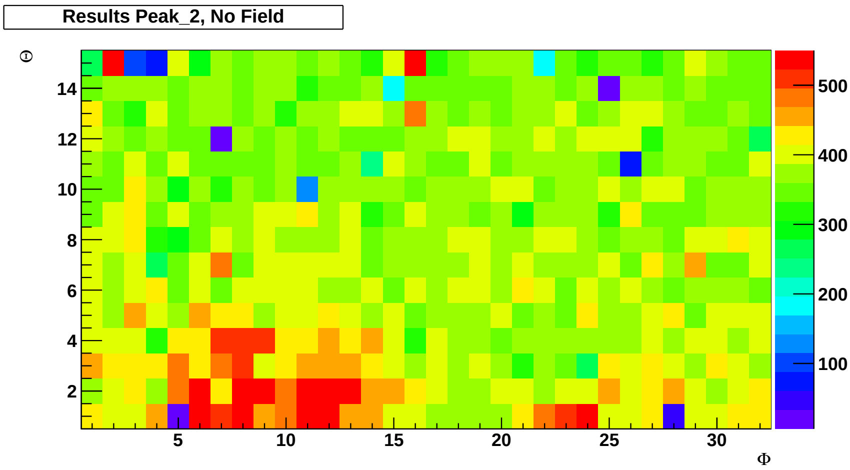

(a) Calibration value *peak_2* of the *BGO* ball without field

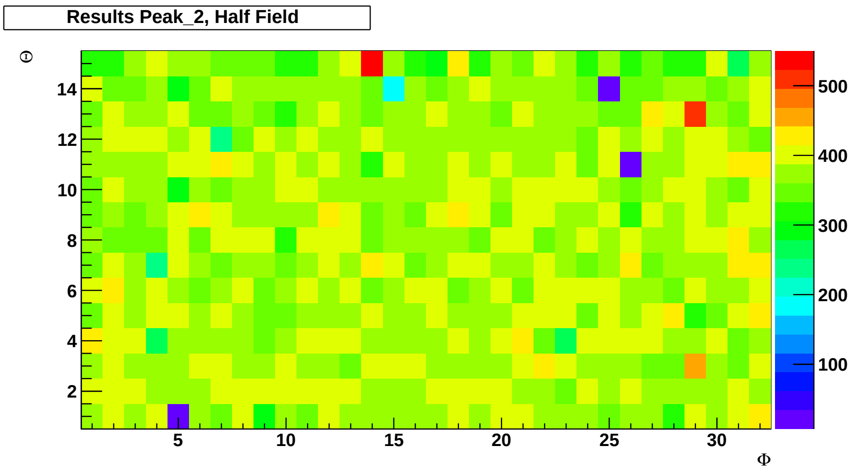

(b) Calibration value *peak_2* of the *BGO* ball with half field

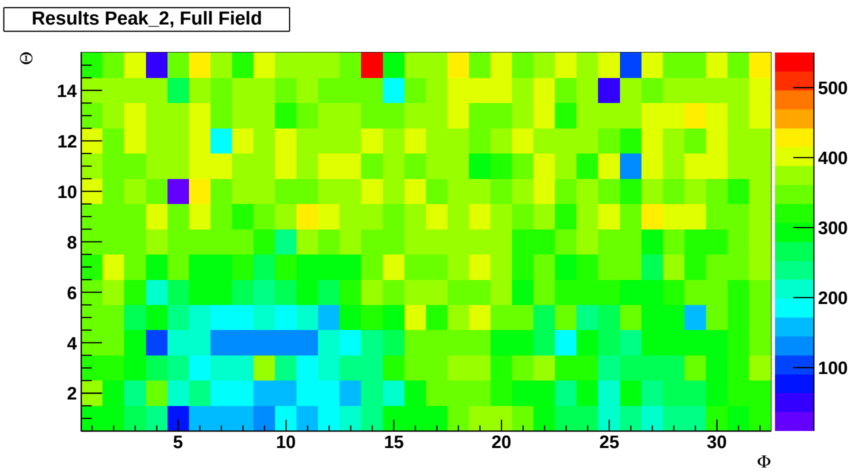

(c) Calibration value *peak_2* of the *BGO* ball with full field

Figure 4.5: Plots of the ADC-responses (*peak_2*) of all channels with the shielding in place: In comparison to fig. 2.8, the improvement can be seen.

4.2 Impact on The Photomultiuplier Tubes' Efficiency

Having installed the magnetic shielding as described in the previous chapter, calibration runs were taken as described in section 2.1. From the resulting mean values for the second peak in the ^{22}Na spectrum, as shown in figure 4.5, one can see a remarkable difference to the former situation, as shown in figure 2.8: Whilst in the unshielded set-up, at full field the central-upper PMTs lost as much as 80 % of efficiency compared to the average PMT in use, the loss when using the shielding is rather 50 %, enough for the photomultiplier tubes to stay operational. Beside the installation of the shielding, a new equalisation at half field strength was undertaken—the reason why without field, the upper-front PMTs are above the average, since they are slightly overcompensating the loss induced by the magnetic field.

In order to examine the "pure" effect of the shielding alone, the plot given in figure 4.6 shows, for each *BGO*-channel, the ratio between the *peak_2*-position without shielding divided by the position with shielding. In both cases, a higher number represents a higher ADC-value, hence the decline in the ratio seen in the lower-left corner of the plot is to be interpreted as the improvement in signal seen by the respective PMTs—which are those just under the shielding.

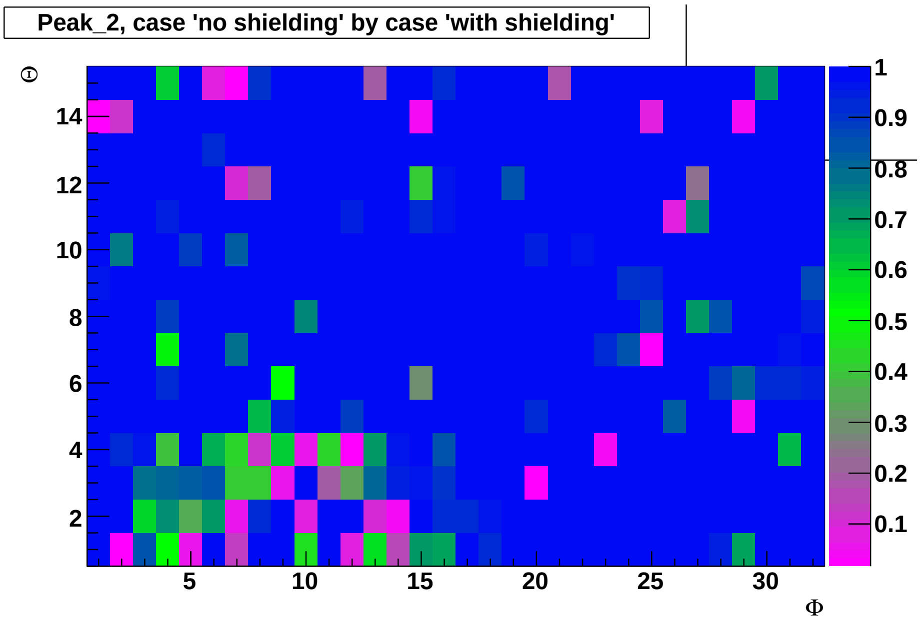

Figure 4.6: Relative change in ADC counts for the second ^{22}Na-peak caused by the installation of the shielding

Due to experimental constraints, the data for this analysis was taken before the shielding was re-arranged to its final design. Nonetheless, it is a more direct way to see that the shielding has a noticeable impact on the PMTs performance. It is seen that the situation improves, however the absolute ADC values were not as good as expected. Therefore, the central 12 bars of the shielding were moved upstream and connected to the girders by additional iron plates. A simulation carried out on the issue underlined the outstanding importance of a conductive connection between the shielding and the other magnetisable parts of the installation.

Another approach to telling apart the influence of the shielding from the difference made by re-equalising with half field, and a way to study the final shielding's effect is based on the following concept: After equalisation, PMTs that suffer more from any distortion (the external field, in this case), will be provided with a higher *set*-value for the high voltage power supply. The better the PMTs are shielded from distorting influences, the smaller is their required HV *set*-value, as seen in figure 4.5b. By comparing two equalisations, one carried out before and one after the installation of the shielding, and both at the same field,[7] the shielding's efficiency can be investigated. The runs carried out in July/August 2014—after the installation of the shielding—in general used a slightly higher HV supply for all crystals than in December 2013, when the equalisation with half field was done without shielding.

Figure 4.7 depicts the relative change in HV-*set*-values for an equalisation, caused by the shielding. Those tubes that suffered most before, $3 \lesssim \Phi \lesssim 13$, could be set to a high voltage about 0.5 to 3.5% less than without the shielding, whilst the other channels were set to up to 2.5 % higher HV values for equalisation.

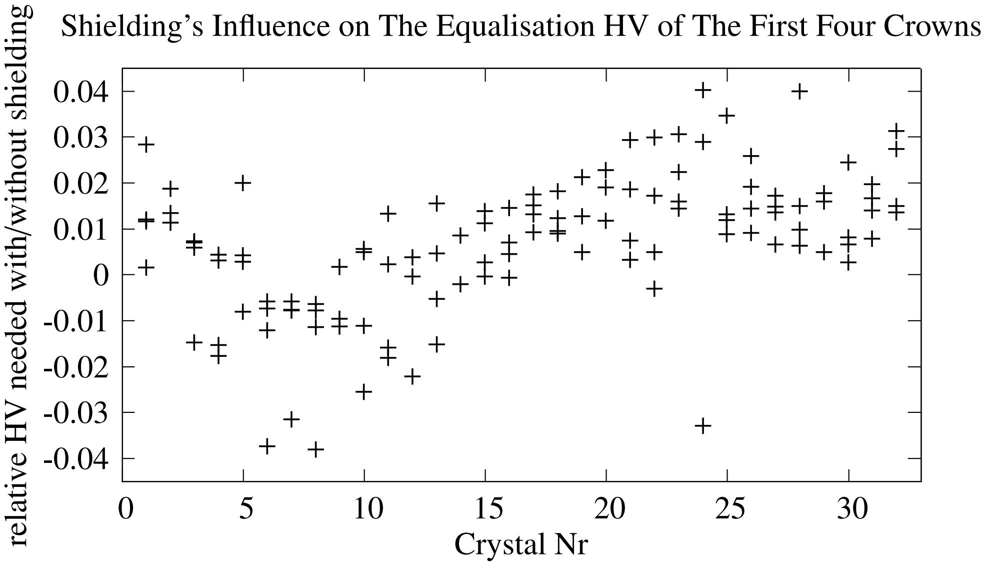

Figure 4.7: Comparison of the supply voltages needed for all *BGO*-PMTs of the four first crowns, after equalisation with half field, value *before* the installation of the shielding relative to the value *afterwards*.

[7] in this case: half field, 216 mT

PMT Voltages

In order to verify whether or not the PMTs can be operated at full field but with shielding, the HV_set values were analysed. During the equalitsation process, the PMTs supply voltages are calculated using a phenomenological formula, that gives a good estimate on the HV value needed for matched gain. Table 4.3 shows, for the front-central PMTs, the HV_set value that is expected for equalisation at full field.

PMT #	Set HV / V	Peak_2 value / ADC channels	estimated HV needed / V
106	1476	158	1604
107	1591	161	1716
108	1734	150	1869
109	1712	135	1863
110	1486	184	1590
206	1412	241	1476
207	1517	196	1612
208	1451	191	1550
209	1381	157	1509
210	1413	159	1540
306	1475	185	1578
307	1451	210	1535
308	1538	207	1625
309	2100	373	2099
310	1526	241	1590
406	1696	224	1771
407	1794	128	1953
408	1588	134	1740
409	1514	135	1665
410	1785	136	1935

Table 4.3: For selected PMTs, the estimated HV needed for equalisation at full field is shown

The assumed voltage needed for equalisation is below the photomultiplier tubes' allowed maximum voltage for 79 % of the tubes investigated. The tubes in the first crown significantly exceed the required values (1700 V for the model used here), the other tubes match the requirements.

CHAPTER 5

Summary & Outlook

To investigate the structure of nucleons and baryons at energies up to 3.5 GeV, the *BGO-OD* experiment is set up at the *ELSA* accelerator facility in Bonn. It is designed for the detection of charged and uncharged mesons in photoproduction processes with real photon-beams. Complementary to the *CB-ELSA/TAPS*-experiment at the same facility, and other set-ups such as *CLAS* or *LEPS*, the *BGO-OD* experiment's set-up is sensitive to charged particles since it combines the hermetic $Bi_4\,Ge_3\,O_{12}$ calorimeter barrel with a magnetic spectrometer in forward direction. One experimental challenge in this unprecedented configuration is to shield the photomultiplier tubes used at the calorimeter barrel from the fringe field of the forward spectrometer's open dipole magnet.

For this thesis, a magnetic shielding for the *BGO-OD* experiment was built (cf. fig. 3.3) and successfully set up at the facility. By simulation, it was shown that the spectrometer's magnetic field has been drawn away from the central part of the calorimeter so that the photomultiplier tubes used in the experiment are less affected by the magnet's fringe field. This effect could be seen in the experimental data, as the average response of the photomultiplier tubes in the *BGO*-calibration runs improved after the installation of several iron bars at the calorimeter (cf. section 4.2). Together with the re-equalisation of the *BGO*-ball, the photomultiplier tubes are now functional even at the full field. Hence, the forward spectrometer can be operated with higher accuracy, using the magnet's full field strength to curve the particles' trajectories.

In addition, it was investigated how the installation of the shielding affects the experiment's momentum reconstruction, as carried out by the forward spectrometer. The analysis presented verifies, that the shielding does not detract the forward spectrometer's reconstruction algorithm and that the newly installed magnetic shielding material, albeit deforming the spectrometer's magnetic field at a crucial area close to the interaction point, does not need special corrections in the analysis. Furthermore, investigations on the forward spectrometer's performance on the momentum reconstruction of particles were undertaken. It was concluded, that the momentum fitting is—on small scales—stable towards general shifts in the magnetic field strength and that the overall width of the reconstructed momenta (for protons) is better than 2 % for particles of 1.2 GeV or higher momentum, whilst being about 3 % at the lower momentum threshold.

Even though the shielding applied seems to be functional, the analysis indicates possible space for improvement. More magnetisable material could be added on top of the shielding's bars and the conductive connection between the shielding and the *BGO*-ball's holding frame could be improved further.

For the momentum reconstruction, a more precise knowledge of the magnetic field's shape could be beneficial. One possible solution to that is its investigation with the help of a high-precision hall probe moved through the fringe field area, position-controlled by a laser-tracker device. Substantial efforts have been undertaken in order to achieve this measurement, it has not been carried out yet.

APPENDIX A

Shielding of Magnetic Fields

The magnetic behaviour of steels varies considerably, depending on the composition of their alloy and their crystalline structure. Typically, the relative permeability, μ/μ_0, of steel ranges from 2420 to 3800 whilst for unalloyed iron, it can be as high as 40,000 for carbonyl iron (99.99 Fe) [15]. "Steel" here refers to structural steel, EN-S275JR, which is also known as St44-2 or AISI-1020; It contains 0.18-0.23$\%_{\text{weight}}$ carbon, 0.30-0.60$\%_{\text{weight}}$ manganese, 0.04$\%_{\text{weight, max}}$ phosphorus and 0.05$\%_{\text{weight, max}}$ sulfur [16] and is mostly used for all construction parts.

Highly permeable materials don't block the magnetic field, as an electric shielding does, but rather draw the field into themselves. Hence, a path for the magnetic field lines around the volume to be shielded is created. *Nonretentive*, i. e. magnetically soft materials, such as highly pure iron (e. g. carbonyl iron), low-carbon and silicon steels, Fe-Ni alloys (e. g., Mumetal®), hexagonal ferrites, and synthetic garnets, are characterised by a high magnetic permeability and a high saturation induction and a low coercivity. Therefore, this class of ferromagnetic materials can be magnetized with a small magnetic field, and hence they are well-suited for electrical applications such as solenoids, transformers and magnetic shielding.

From the simulation, as mentioned in section 2.2, it was learned that the *BGO* holding structure serves as a "magnetic shielding" for the photomultipliers. Its effect can be studied in figure 3.5: In the upper half, the magnetic field is as strong as 45 mT, and has a relatively regular shape—while below the centre (the beam axis), the field is both, weaker and deformed at both sides.

To get an impression on how the fringe field is affected by the steel holding structure, figure A.1a shows the magnetic field at the most critical position. It is seen that the metallic stands draw the field in a new direction. Figure A.1b shows the simulated effect of the new designed shielding structure on the magnetic field: The field lines are drawn from the central volume into the steel bars attached above the multiplier tubes; At the bars, the field strength can top 400 $\mathrm{mV\,s\,m^{-2}}$. In the central-upper position, where in the unshielded situation [A.1a] the field strength was about 4.4 mT it is decreased to less than 2 mT [A.1b], much closer to the $\lesssim 1$ mT simulated for the lower part of the first *BGO* crowns.

If not noted otherwise, field strengths are referred to as strengths of the absolute magnetic field. This is mainly because (a) the fringe field at this distance has one dominant component and (b) since the individual orientations of the PMTs are not taken into consideration/simulation, a more particular knowledge on the field's direction is unneeded.

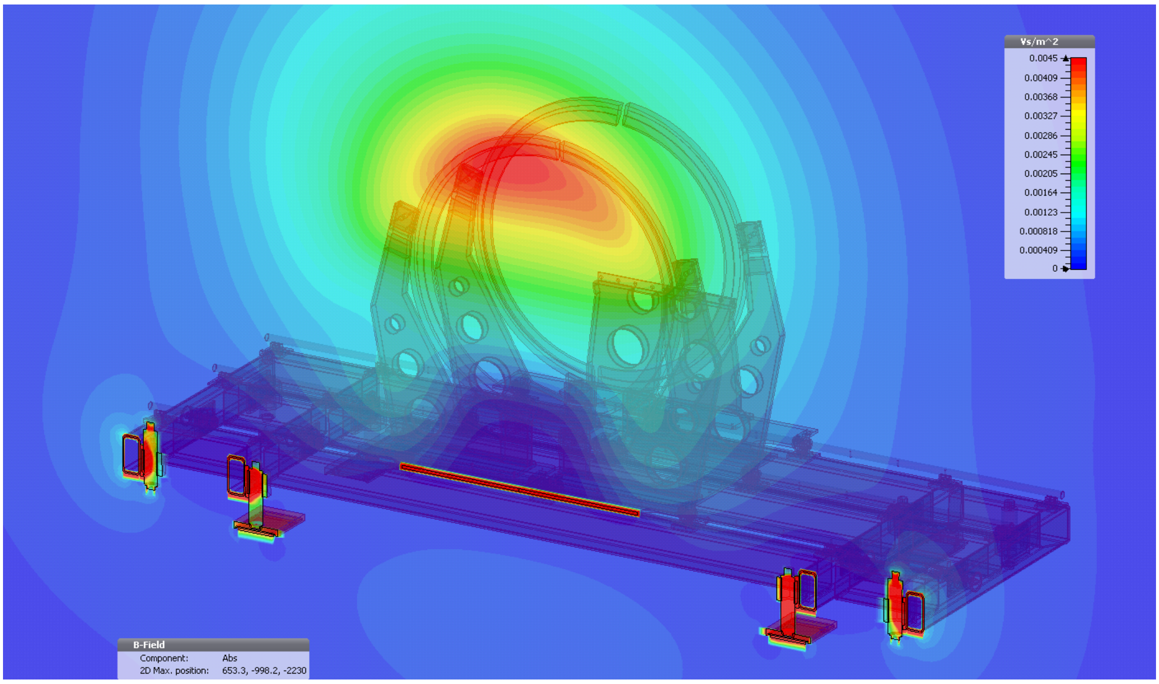

(a) The positioning of the field map shown in fig. 3.5

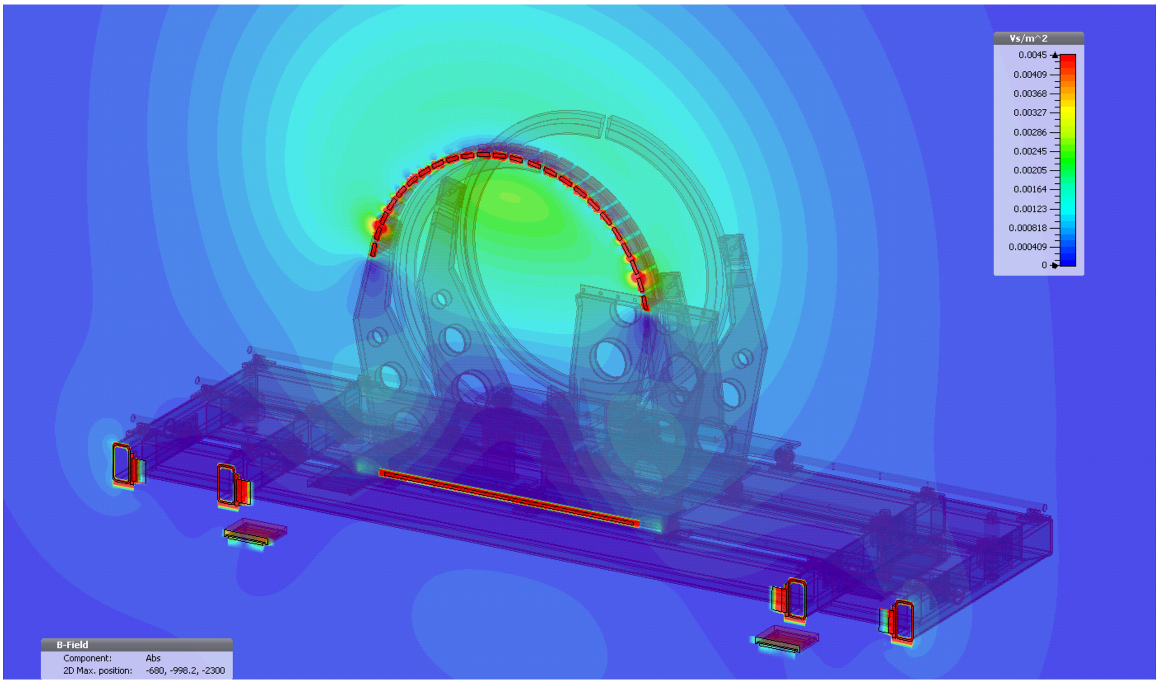

(b) The shielding's effect on the fringe field can be seen in this field map

Figure A.1: The two field maps allow to see the shielding's impact on the (absolute) magnetic field.

APPENDIX B

Momentum Reconstruction

The forward spectrometer of the *BGO-OD* experiment is responsible for the momentum reconstruction of the charged particles ejected at forward angles. Particle trajectories are curved in the field of the open dipole magnet, and tracking detectors measure these trajectories. Momentum reconstruction is done in a two-step manner, first track finding routines are used, then algorithms to determine particle momenta are implemented.

Track Finding

Tracks are reconstructed on both sides of the magnet, as figure B.1 illustrates: The so-called "front-tracks" are made from the energy deposition in MoMo and SciFi2, and the "rear tracks" are found using the eigth drift chambers' signals.

While SciFi2, using a grid of crossed scintillator fibres, cannot disentangle ghost-hits, together with MoMo's geometry, events can be reduced to very few candidate tracks. Demanding that tracks must originate from the target selects correct combinations of tracks fom SciFi2 and MoMo. By fitting a straight line to these tracks (as the fringe field is orders of magnitude lower than the field inside the magnet), a first guess of the particles' trajectories is made. For the rear tracks, all entries in the drift chambers are analysed, first combining clusters of all eight drift chamber channels, if possible, than requiring only seven hits for a track, than six and so forth. Finally, a set of front- and rear tracks is found.

Combinations of front and rear tracks are usual to form complete tracks. It is required to check whether or not the tracks found are meaningful physics-wise. Two cuts are in place to do this. In the x-y-plane, the tracks are bound to not pass through the magnet's yoke, e g. their point of intersection may not be located far outside the magnet's air-filled gap. In the y-z-plane, the tracks may not be curved (since the particles do not experience Lorentz' force in this dimension) and may not be discontinuous or otherwise skewed. If the reconstructed tracks fulfil these criteria, they are combined as a complete, curved track.

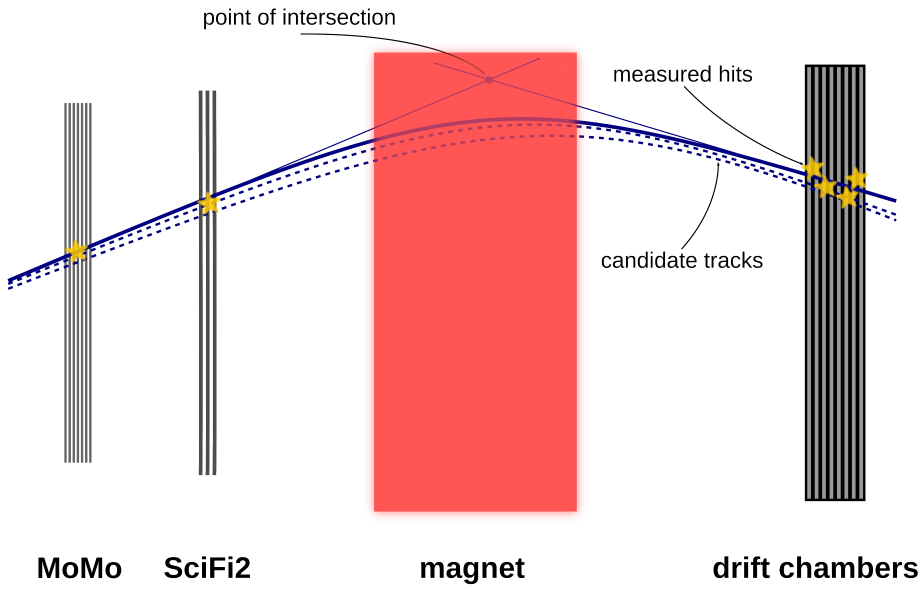

Figure B.1: Schematic sketch of the momentum reconstruction: From the hits measured, possible candidate tracks are derived. By an iterative approach, the best fit for the momentum in order to reconstruct the particle's track is found.

Momentum Measurement

Assuming the magnetic field to be homogeneous in one part of the area and zero everywhere else, together with the front- and rear track of a particle found as described above, a rough first estimate on the momentum is made. From this guess, simulating the path of the particle trough the set-up and calculating its expected energy loss due to scattering[1] in air and the detectors, and then comparing the resulting positions to the measured ones. The momentum reconstruction is iteratively improved to an accuracy of about 3 %.

In order to obtain more precise momentum measurements, the tracks and the reconstructed momentum are used as an input to the analysis tool called "GenFit". It makes use of the geometry and drift time of the drift chambers and the SciFi fibre arrangement to gain a better spatial resolution. For that purpose, it breaks the tracks apart and uses the drift times in the drift chambers or the overlapping geometry in the scintillator fibres. Thus, a final momentum resolution of 1.5 % can be achieved.

[1] It is required to have a first assumption on the particle's momentum and particle type—e. g. proton, kaon, pion and so forth—since the energy loss as described by the Bethe formula [17] changes with these properties.

Explora & GenFit

For reconstruction of particles, the *BGO-OD* experiment makes use of a programme suite called "ExPlORA", short for "Extended Pluggable Object-oriented ROOTified Analysis". It is organised by a collection of XML files, providing an interface for ROOT and GEANT4 which easily allows event-based analysis as well as data visualisation. Beside analysis of experimental data, ExPlORA, together with its GEANT4 bindings, is used for the simulation of particles and their behaviour in the experiment and DAQ.

GenFit is an extension to ExPlORA's momentum reconstruction algorithm that improves the accuracy by splitting the clusters into their individual hits. Fitting the reconstructed tracks to the single hits and minimising the candidate tracks' χ^2 with respect to the hits, a more precise momentum measurement can be obtained. Details of the momentum reconstruction are described by P.-F. Hartmann in his master thesis [18].

APPENDIX C

Influence of Over- And Under-Estimated Magnetic Fields

As described in section 3.3, it was investigated how a deviation between the field strength the reconstruction algorithm uses and the actual field strength in the *BGO-OD* experiment influences the momentum reconstruction. To do so, all values for the fields read in were modified (by ± 10 and ± 3 %) towards the "original" field strength used for particle simulation. Then, protons of all energies were simulated and reconstructed (using wrong field strengths).The resulting momentum was than compared to the momentum used in the simulation.

Figure C.1 shows the result: From the fact that the reconstructed particles are distributed around straight lines with slope zero, it can be understood that the momentum reconstruction is essentially independent from the protons' energies. From the positioning of these lines, the offset in the reconstructed momentum can be learned, which is the y-intercept of the distribution's centre. Since the slope is negligible, the y-intercept can be measured by projecting the values on the y-axis and fitting a Gauß-function on the projection.

This is done in the plots shown in figure C.2. The peak centre can be interpreted as the offset to the reconstructed momentum induced by the shift in assumed magnetic field strength that was taken for the simulation. The four peaks' mean values are plotted versus the magnetic field shift in figure 4.1. Furthermore, the reconstruction width, σ, shrinks with higher field, as expected, but seems to be unaffected by the induced mis-estimation of the magnetic field.

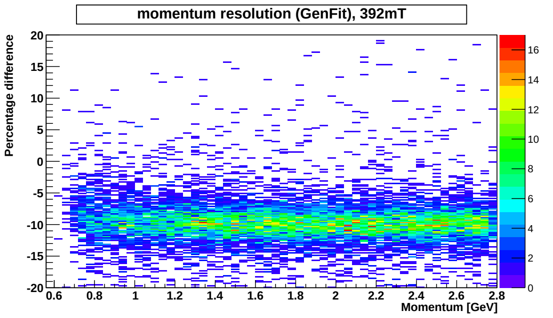

(a) The momentum resolution difference between simulation and reconstruction for a reconstruction field shift of −10 %

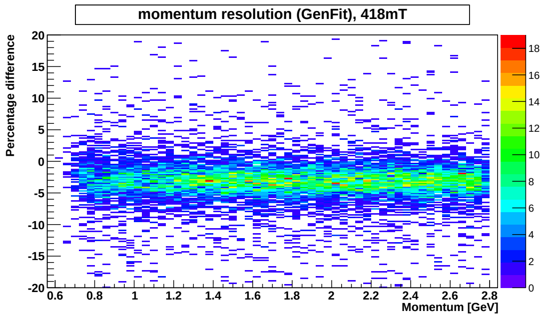

(b) The momentum resolution difference between simulation and reconstruction for a reconstruction field shift of −3 %

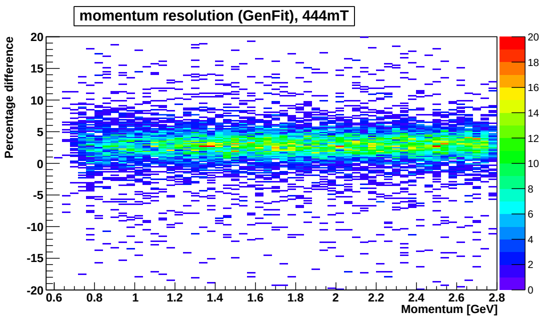

(c) The momentum resolution difference between simulation and reconstruction for a reconstruction field shift of +3 %

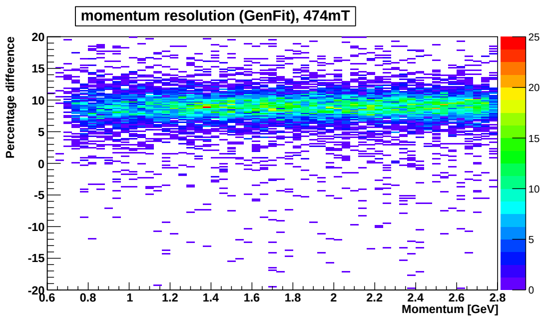

(d) The momentum resolution difference between simulation and reconstruction for a reconstruction field shift of +10 %

Figure C.1: The momentum reconstruction offset (y-axis) is independent from the simulated proton energy (x-axis), but shifts with the error in the assumed magnetic field strength.

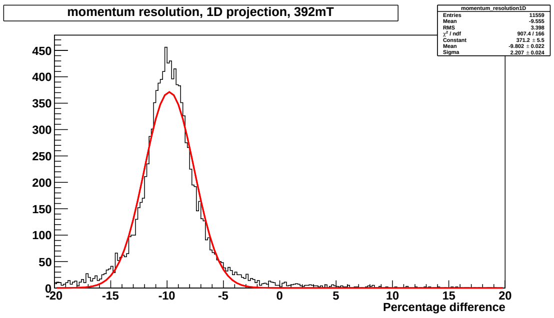

(a) 1D-Projection of fig. C.1a (−10 %)

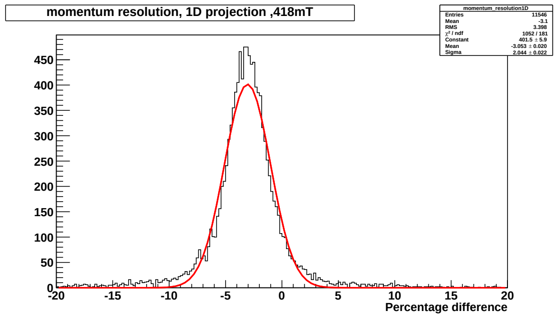

(b) 1D-Projection of fig. C.1b (−3 %)

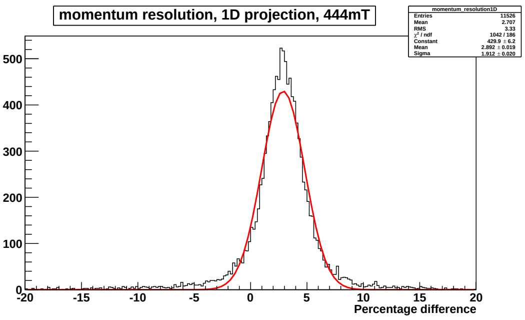

(c) 1D-Projection of fig. C.1c (+3 %)

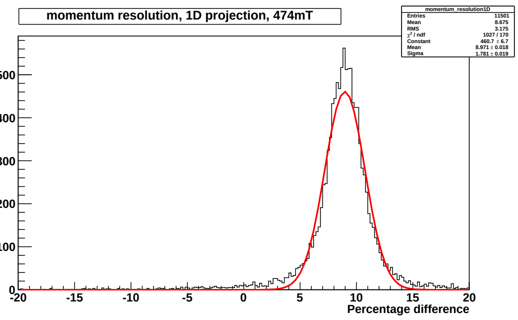

(d) 1D-Projection of fig. C.1d (+10 %)

Figure C.2: The projections of the plots C.1 reveal information about how much the momentum reconstructed deviates from the “real” momentum of a particle, if the magnetic field is over- or under-estimated.

Bibliography

[1] Henry Way Kendall,
Deep Inelastic Scattering: Experiments on the Proton and the Observation of Scaling,
accessed July 6, 2014,
1990,
URL: http://www.nobelprize.org/nobel_prizes/physics/laureates/1990/kendall-lecture.pdf.

[2] J. Beringer et al.,
"Review of Particle Physics",
In: *Phys. Rev. D* 86 (1 July 2012) 010001,
DOI: 10.1103/PhysRevD.86.010001,
URL: http://link.aps.org/doi/10.1103/PhysRevD.86.010001.

[3] G. Aad et al.,
"Observation of a new particle in the search for the Standard Model Higgs boson with the ATLAS detector at the LHC",
In: *Physics Letters B* 716.1 (2012) 1–29,
ISSN: 0370-2693,
DOI: http://dx.doi.org/10.1016/j.physletb.2012.08.020,
URL: http://www.sciencedirect.com/science/article/pii/S037026931200857X.

[4] V. Vegna,
"Photoproduction of Vector Mesons",
In: *Journal of Physics: Conference Series* 349 (1 2012),
DOI: 10.1088/1742-6596/349/1/012016.

[5] T.C. Jude,
"Status and perspectives in strangeness photoproduction",
In: *Journal of Physics: Conference Series* 349.1 (2012) 012006,
DOI: doi:10.1088/1742-6596/349/1/012012,
URL: http://stacks.iop.org/1742-6596/349/i=1/a=012006.

[6] V Vegna and J Hannappel,
Vector Meson Photoproduction at BGO-OD,
2012,

URL: http://bamboo.pv.infn.it/DBmambo/DBdoc/ELSA-04-2012-BGO.pdf.

[7] R. Ewald et al.,
"Anomaly in the photoproduction cross section off the proton at the threshold",
In: *Physics Letters B* 713.3 (2012) 180–185,
ISSN: 0370-2693,
DOI: http://dx.doi.org/10.1016/j.physletb.2012.05.066,
URL: http://www.sciencedirect.com/science/article/pii/S0370269312006259.

[8] E. J. Williams,
"Nature of the High Energy Particles of Penetrating Radiation and Status of Ionization and Radiation Formulae",
In: *Phys. Rev.* 45 (10 May 1934) 729–730,
DOI: 10.1103/PhysRev.45.729,
URL: http://link.aps.org/doi/10.1103/PhysRev.45.729.

[9] H. A. Bethe,
"The influence of screening on the creation and stopping of electrons",
In: *Mathematical Proceedings of the Cambridge Philosophical Society* 30 (04 Oct. 1934) 524–539,
ISSN: 1469-8064,
DOI: 10.1017/S0305004100012779,
URL: http://journals.cambridge.org/article_S0305004100012779.

[10] P. Levi Sandri et al.,
"Performance of a *BGO* calorimeter in a tagged photon beam from 260 to 1150 MeV",
In: *Nuclear Instruments and Methods in Physics Research Section A: Accelerators, Spectrometers, Detectors and Associated Equipment* 370.2–3 (1996) 396–402,
ISSN: 0168-9002,
DOI: http://dx.doi.org/10.1016/0168-9002(95)00839-X,
URL: http://www.sciencedirect.com/science/article/pii/016890029500839X.

[11] S. Eidelmann et al.,
Particle Physics Booklet,
July 2004.

[12] F. Ghio et al.,
"The *GRAAL* high resolution *BGO* calorimeter and its energy calibration and monitoring system",
In: *Nuclear Instruments and Methods in Physics Research Section A: Accelerators, Spectrometers, Detectors and Associated Equipment* 404.1 (1998) 71–86,
ISSN: 0168-9002,
DOI: http://dx.doi.org/10.1016/S0168-9002(97)01124-8,
URL: http://www.sciencedirect.com/science/article/pii/S0168900297011248.

[13] John David Jackson,
Classical Electrodynamics,

3rd ed.,
John Wiley & Sons, New York, 1999,
ISBN: 0-471-30932.

[14] *Product Flyer: CST EM Studio*,
accessed August 28, 2014,
URL: https://www.cst.com/Content/Media/CST_EMS_low.pdf.

[15] Francois Cardarelli,
Materials Handbook: A Concise Desktop Reference,
2nd ed.,
J. Springer, 2009,
ISBN: 978-1-84628-668-1,
DOI: 10.1007/978-1-84628-669-8.

[16] *Carbon Steel AISI 1020*,
accessed July 20, 2014,
URL: https://www.efunda.com/materials/alloys/carbon_steels/show_carbon.cfm?ID=AISI_1020&prop=all&Page_Title=AISI%201020.

[17] H. A Bethe and J. Ashkin,
"Passage of radiation through matter",
In: *Experimental Nuclear Physics* 1 (1953).

[18] Paul-Fiete Hartmann,
"Momentum reconstruction in the BGO-OD forward spectrometer",
master thesis: University of Bonn, 2014.

List of Figures